Doppler radial velocity detection based on Doppler asymmetric spatial heterodyne spectroscopy technique for absorption lines*

Yin-Li Kuang(况银丽)[1,2], Liang Fang(方亮)[1,†], Xiang Peng(彭翔)[1], Xin Cheng(程欣)[1], Hui Zhang(张辉)[1], and En-Hai Liu(刘恩海)[1]

[1] *Institute of Optics and Electronics, Chinese Academy of Sciences, Chengdu* 610209, *China*
[2] *University of Chinese Academy of Sciences, Beijing* 100049, *China*

(Received 27 September 2019; revised manuscript received 20 November 2019; accepted manuscript online 9 December 2019)

Doppler asymmetric spatial heterodyne spectroscopy (DASH) technique has developed rapidly in passive Doppler-shift measurements of atmospheric emission lines over the last decade. With the advantages of high phase shift sensitivity, compact, and rugged structure, DASH is proposed to be used for celestial autonomous navigation based on Doppler radial velocity measurement in this work. Unlike atmospheric emission lines, almost all targeted lines in the research field of deep-space exploration are the absorption lines of stars, so a mathematical model for the Doppler-shift measurements of absorption lines with a DASH interferometer is established. According to the analysis of the components of the interferogram received by the detector array, we find that the interferogram generated only by absorption lines in a passband can be extracted and processed by a method similar to the approach to studying the emission lines. In the end, numerical simulation experiments of Doppler-shift measurements of absorption lines are carried out. The simulation results show that the relative errors of the retrieved speeds are less than 0.7% under ideal conditions, proving the feasibility of measuring Doppler shifts of absorption lines by DASH instruments.

Keywords: Doppler asymmetric spatial heterodyne spectroscopy (DASH), Doppler-shift measurement, absorption line, celestial autonomous navigation

PACS: 07.60.Ly, 42.87.Bg, 47.80.Cb **DOI:** 10.1088/1674-1056/ab5fc3

1. Introduction

Navigation of spacecraft is a key technology in deep space explosion fields. Terrestrial radio navigation,[1–3] as the mainstream navigation technology, has the shortcomings of being easily occluded by other celestial bodies and the huge communication delay between earth-based TT & C (Telemetry, Tracking, and Command) stations and deep space detectors. Celestial autonomous navigation with good real-time and high navigation accuracy capability has become a trend in the development of deep space navigation technology. The celestial autonomous navigation based on Doppler radial velocity measurement has been proposed for directly acquisting the velocity[4] and eliminating the adverse effects of differential on velocity accuracy in the inertial navigation[5] and the celestial autonomous navigation based on angle measurement.[6–8]

In the celestial autonomous navigation based on Doppler radial velocity measurement, the space velocity of the spacecraft in inertial space can be determined from the radial velocities between the spacecraft and the stars, combined with celestial ephemeris and spacecraft inertial attitude information. Doppler-shift measurements of the star spectral lines with a spectroscopic instrument on board provide radial velocities. Among the existing spectroscopic instruments for passive Doppler radial velocity measurements, Fabry–Perot interferometers,[9,10] stepped Fourier transform spectrometers (FTS)[11–17] and Doppler asymmetric spatial heterodyne spectroscopy (DASH) interferometers meet the mass and volume requirements of spaceborne detectors for deep-space exploration, while Fabry–Perot interferometers strictly require processing precision and alignment accuracy, which makes it have a small tolerance range and thus it is not the most suitable candidate. Compared with stepped FTS, DASH interferometers without slits cannot only sample all optical path differences at the same time without any moving parts, but also measure multiple lines simultaneously. With the characteristics of high spectral resolution, high phase shift sensitivity, rugged DASH interferometers are more suitable for deep-space celestial autonomous navigation.

The DASH concept, proposed in 2006,[18] has developed rapidly in the field of passive atmospheric wind measurement. The ground-based Redline DASH Demonstration Instrument (REDDI),[19,20] the space-based atmospheric redline interferometer for dOppler winds (ARROW)[21–23] and Michelson Interferometer for global high-resolution thermospheric imaging (MIGHTI),[24–27] all DASH-based instruments, have been successfully developed and achieved a Doppler radial velocity measurement accuracy of a few meters per second. It is worth

*Project supported by the National Basic Research Program of China (Grant No. 2014CB744204).
†Corresponding author. E-mail: fangl@ioe.ac.cn

noting that in the field of atmospheric wind measurement, the targeted spectral lines detected by a DASH instrument are the emission lines, and the interferogram distribution obtained on the detector is simple and the theory is relatively mature. But in the research field of deep space exploration, targeted lines carrying Doppler-shift information are the absorption lines of stars, and the emission lines are generally not available. There are few reports on the application of DASH technique to the Doppler-shift measurement of absorption lines. Therefore, it is extremely important to establish a set of theories for analyzing and processing the interference patterns obtained with a DASH instrument for absorption lines.

Aiming at the unique characteristics of absorption lines, a mathematical model for the Doppler-shift measurement of absorption lines is established. After the detailed analysis of the intensity distribution of the interferogram received by a detector, we show that the interferogram generated by the absorption lines in the passband can be extracted, and then be processed by a method similar to the approach to studying the emission lines. Furthermore, we numerically simulate the Doppler-shift measurements of some absorption lines in the passband.

2. Doppler shift determination

As shown in Fig. 1, a DASH interferometer typically includes a collimation system, a filter, a beam splitter, two identical blazed gratings, an imaging system, and a detector array. Signal light entering into the DASH interferometer is collimated into a plane wave front through a collimation system. After passing the filter, the plane wave front is divided into two beams with the same intensity by a beam splitter coated with a semi-transparent film, so that the two resulting beams illuminate the blazed gratings fixed at the ends of the interferometer arms. The two beams diffracted at the blazed gratings return to the beam splitter and recombine. Then, the lines whose wavelengths are not equal to the Littrow wavelength of the blazed grating propagate at a small angle with respect to the optical axis. The Fizeau interference fringes whose spatial frequency is proportional to the heterodyne of the wave number σ of incident radiation and the Littrow wave number σ_L of the grating are imaged on the detector array. The magnification of the imaging optics is assumed to be unity. The interferogram can be written as[28]

$$I(L) = \frac{1}{2}\int_0^{\infty} B(\sigma)\left[1+\cos\{2\pi(\sigma-\sigma_L)L\}\right]\mathrm{d}\sigma, \qquad (1)$$

where $B(\sigma)$ is the spectral density of the filtered radiation, $L = 4\tan\theta \times (x + \Delta d/2\tan\theta)$ is the sampling optical path difference, θ is the blaze angle of the blazed grating, $2\Delta d$ is the optical path difference offset between two arms, and x is the position on the detector array ($x = 0$ indicates the center of the detector, where the sampling optical path difference $L = 2\Delta d$). In general, the path difference offset is equal to the optimal optical path difference obtained from the trade-off between interference fringe contrast and phase shift. In theory, it is determined by the full width at half maximum (FWHM) of the targeted line.[29] Generally, a narrower FWHM corresponds to a larger path difference offset.

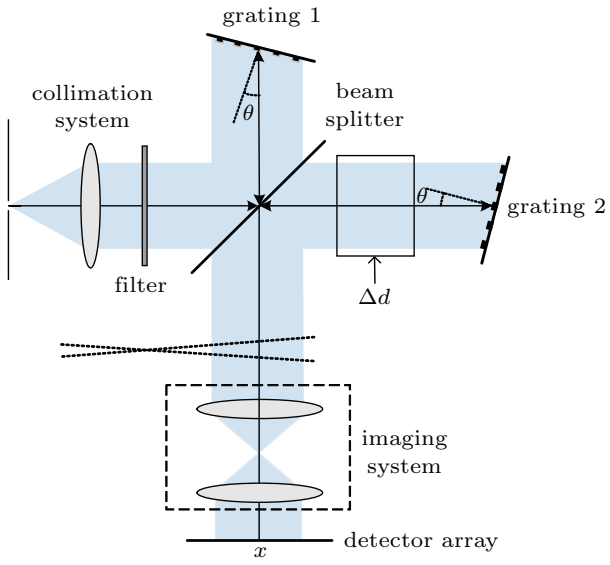

Fig. 1. Schematic diagram of non-field-widened DASH interferometer.

2.1. Single absorption line in passband

After the incident radiation enters into the DASH interferometer, the spectral domain is limited by a filter. Supposing that the transmission function of the filter is a Gaussian function and there is only a single absorption line with a Gaussian line shape in the passband, the spectral density of the filtered radiation $B(\sigma)$, as shown in Fig. 2, can be expressed as

$$B(\sigma) = A_0\exp\left[\frac{-2^2\ln 2\,(\sigma-\sigma_0)^2}{w_0^2}\right] \times\left\{1-A_1\exp\left[\frac{-4\ln 2\,(\sigma-\sigma_1')^2}{w_1^2}\right]\right\}, \qquad (2)$$

where A is the magnitude of the energy within the filter bandpass; A_1 ($0 < A_1 < 1$) is the absorption depth of the absorption line; w is the FWHM of the filter's transmission function; w_1 is the FWHM of the absorption line; σ is the center wave number of the filter's transmission function; σ_1' is the Doppler-shifted center wavenumber of the absorption line, which is a function of Doppler radial velocity v. If the Doppler-non-shifted center wavenumber of the absorption line is σ_1, and the speed of light is c, then $\sigma_1' = \sigma_1\cdot(1+v/c)$. Equation (2) can be abbreviated as follows:

$$B(\sigma) = B_0(1-B_1) = B_0 - B_0B_1, \qquad (3)$$

where $B_0 = A_0\exp[-2^2\ln 2\,(\sigma-\sigma_0)^2/w_0^2]$ and $B_1 = A_1\exp[-4\ln 2\,(\sigma-\sigma_1')^2/w_1^2]$.

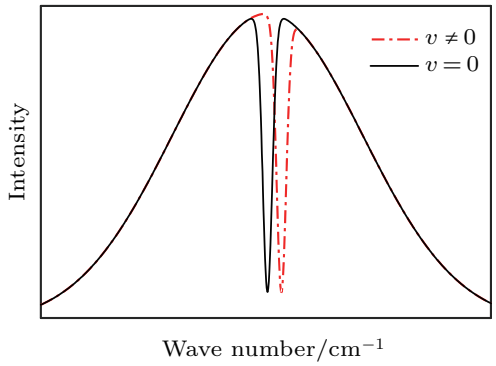

Fig. 2. Doppler shift in incident spectrum.

According to Eqs. (1) and (2), the interferogram of incident radiation received on the detector can be written as

$$\begin{aligned} I(x) = {} & \frac{A_0 w_0}{4}\sqrt{\frac{\pi}{\ln 2}} + \frac{A_0 w_0}{4}\sqrt{\frac{\pi}{\ln 2}} \\ & \times \exp\left(-\frac{L^2\pi^2 w_0^2}{4\ln 2}\right)\cos\left(2\pi L(\sigma_0-\sigma_L)\right) \\ & - \frac{A_0 A_1 w_0 w_1}{4\sqrt{w_0^2+w_1^2}}\sqrt{\frac{\pi}{\ln 2}}\exp\left(-\frac{4\ln 2(\sigma_0-\sigma_1')^2}{w_0^2+w_1^2}\right) \\ & - \frac{A_0 A_1 w_0 w_1}{4\sqrt{w_0^2+w_1^2}}\sqrt{\frac{\pi}{\ln 2}}\exp\left(-\frac{4\ln 2(\sigma_0-\sigma_1')^2}{w_0^2+w_1^2}\right) \\ & \times \exp\left(-\frac{L^2\pi^2 w_1^2 w_0^2}{4\left(w_0^2+w_1^2\right)\ln 2}\right) \\ & \times \cos\left(2\pi L\left(\frac{w_1^2\sigma_0+w_0^2\sigma_1'}{w_0^2+w_1^2}-\sigma_L\right)\right). \end{aligned} \tag{4}$$

This formula contains two constant terms and two cosine terms. These two cosine terms can be explained as the superposition of two sets of interference fringes with different spatial frequencies, which are different from the scenario of the interferogram of a single emission line with only one spatial frequency. The first set of interference fringes described by the first cosine term in Eq. (4) is generated by the transmission function which is indicated by B_0, and its interference fringe contrast is determined by the envelope function $E_0 = = \exp(-L^2\pi^2 w_0^2/4\ln 2)$. The second set of interference fringes described by the second cosine term in Eq. (4) is generated by B_0B_1, and its interference fringe contrast is determined by the envelope function $E_1 = \exp(-L^2\pi^2 w_0^2 w_1^2/4\left(w_0^2+w_1^2\right)\ln 2)$. It can be seen from the expression of envelope functions E_0 and E_1 that the contrast between the two sets of interference fringes decreases exponentially with the increase of the optical path difference L. In general, when the interference fringe contrast drops to 1/e, the corresponding optical path difference is defined as the coherence length. After the targeted radiation enters into the DASH interferometer, the interference pattern can be obtained when the difference in optical path between the two coherent beams is less than the coherence length. Therefore, the optical path difference L_{c0} that makes $E_0 = e^{-1}$ is defined as the coherence length of B_0, then $L_{c0} = 2\sqrt{\ln 2}/\pi w_0$. Similarly,

$$L_{c1} = \frac{2\sqrt{\left(w_0^2+w_1^2\right)\ln 2}}{\pi w_0 w_1} = \frac{\sqrt{\left(w_0^2+w_1^2\right)}}{w_1}L_{c0} = \sqrt{m^2+1}L_{c0}$$

(where $w = mw_1$) is the coherence length of B_0B_1. Therefore, without considering the constant term component, the intensity distribution of interference fringes in the region of $|L| < L_{c0}$ is the result of superposition of the first set of interference fringes and the second set of interference fringes, while in the region of $L_{c0} < |L| < L_{c1}$, it is described only by the second cosine term. It is worth noting that only the second cosine term contains Doppler shift information. So, the Doppler shift of the absorption line in the passband can be determined from the phase shift of the interference fringes in the region of $L_{c0} < |L| < L_{c1}$. In order to obtain the highest phase shift sensitivity, the sampling optical path difference L at $x = 0$ on the detector is generally selected as

$$L_{opt} = 2\Delta d = \frac{\sqrt{2\left(w_0^2+w_1^2\right)\ln 2}}{\pi w_0 w_1} = \sqrt{\frac{m^2+1}{2}}L_{c0} = \frac{1}{\sqrt{2}}L_{c1}$$

(where $w = mw_1$), which is obtained by maximizing the efficiency function[29] $P = LE_1$. Since $m > 2$ in general, L_{opt} is in the region of $L_{c0} < |L| < L_{c1}$. In this way, the interference fringes near the center of the detector are generally generated by the absorption line in the passband.

Therefore, the interferogram generated by the absorption line in the passband can be extracted from the interferogram described in Eq. (4) and written as

$$\begin{aligned} I(x) \approx {} & \frac{A_0 w_0}{4}\sqrt{\frac{\pi}{\ln 2}} - \frac{A_0 A_1 w_0 w_1}{4\sqrt{w_0^2+w_1^2}}\sqrt{\frac{\pi}{\ln 2}} \\ & \times \exp\left(-\frac{4\ln 2(\sigma_0-\sigma_1')^2}{w_0^2+w_1^2}\right) - \frac{A_0 A_1 w_0 w_1}{4\sqrt{w_0^2+w_1^2}}\sqrt{\frac{\pi}{\ln 2}} \\ & \times \exp\left(-\frac{L^2\pi^2 w_0^2 w_1^2}{4\left(w_0^2+w_1^2\right)\ln 2} - \frac{4\ln 2(\sigma_0-\sigma_1')^2}{w_0^2+w_1^2}\right) \\ & \times \cos\left(2\pi L\left(\frac{w_1^2\sigma_0+w_0^2\sigma_1'}{w_0^2+w_1^2}-\sigma_L\right)\right). \end{aligned} \tag{5}$$

This interferogram is very similar to that of a single emission line. So the retrieved phases of interference fringes can be calculated by following the approach to studying the atmospheric emission lines.[28] Then the phase shift at $x = 0$ can be obtained by subtracting the zero Doppler radial velocity phase, and the resulting expression is as follows:

$$\Delta\Phi = 4\pi\Delta d\frac{w_0^2}{w_0^2+w_1^2}\sigma_1\cdot\frac{v}{c}. \tag{6}$$

Thus, the Doppler radial velocity v can be solved from Eq. (6) as

$$v = \frac{w_0^2 + w_1^2}{w_0^2} \frac{c}{\sigma_2} \frac{\Delta\Phi}{4\pi\Delta d}. \tag{7}$$

If w^2 is much larger than w_1^2, which means that ignoring the influence of the transmission function of the filter on the spectral density of the targeted absorption line, the above equation can be simplified into

$$v = \frac{c}{\sigma_2} \frac{\Delta\Phi}{4\pi\Delta d}. \tag{8}$$

In practice, the transmission function of the filter we chose is mostly wide enough, and then has a negligible effect on the absorption line of interest. So, equation (8) can be used to calculate the retrieved Doppler radial velocity. Under this condition, the relationship between the Doppler radial velocity and the phase shift is the same as that in the case of an emission line.

2.2. Multiple absorption lines in passband

In general, there are several absorption lines in a stellar spectral passband. Presuming that all of those have Gaussian line shapes, we can simplify the interferogram recorded on the detector by writing as:

$$\begin{aligned} I_{\mathrm{DM}}(x) = {} & \frac{A_0 w_0}{4}\sqrt{\frac{\pi}{\ln 2}} + \frac{A_0 w_0}{4}\sqrt{\frac{\pi}{\ln 2}} \\ & \times \exp\left(-\frac{L^2\pi^2 w_0^2}{4\ln 2}\right)\cos\left(2\pi L(\sigma_L - \sigma_0)\right) - \sum_j S_j \\ & - \sum_j S_j \cdot E_j \cos\left(2\pi L\left(\frac{w_0^2\sigma_j' + w_j^2\sigma_0}{w_0^2 + w_j^2} - \sigma_L\right)\right), \end{aligned} \tag{9}$$

where j indexes several absorption lines in the passband, S_j is a constant coefficient, E_j is the envelope function that depends on the individual FWHM w_j which is much narrower than w, L_{cj} is the coherence length calculated from $E_j = \mathrm{e}^{-1}$. Based on the analysis in Subsection 2.1, in the region of $L_{c0} < |L| < L_{cs}$ (where L_{cs} is the smallest in L_{cj}) the first cosine term in Eq. (9) can be ignored. Then equation (9) can be rewritten as

$$\begin{aligned} I_{\mathrm{DM}}(x) = {} & \frac{A_0 w_0}{4}\sqrt{\frac{\pi}{\ln 2}} - \sum_j S_j - \sum_j S_j \cdot E_j \\ & \times \cos\left(2\pi L\left(\frac{w_0^2\sigma_j' + w_j^2\sigma_0}{w_0^2 + w_j^2} - \sigma_L\right)\right). \end{aligned} \tag{10}$$

This interferogram can also be treated as an interferogram from multiple emission lines. It is possible to perform the independent velocity measurement of all absorption lines in the passband by repeating the procedure used for a single emission line. Besides, if there are numerous absorption lines that are too densely distributed to be well distinguished in frequency domain, it will do to treat them as one spectral line at low spectral resolution.[29] After getting the phase shift, we can calculate the retrieved speed according to Eq. (8).

3. Numerical simulation

Doppler-shift measurement of a single absorption line in the passband is simulated numerically under ideal conditions. Table 1 gives specifications of the targeted absorption line and the DASH interferometer. Here, both the absorption line and the transmittance function of the filter have Gaussian line shapes, and their FWHMs are 0.01 nm and 1 nm, respectively. It is assumed that the Doppler radial velocity between the signal source and the DASH interferometer is 100 m/s. The optical path difference offset is taken as 6.40 mm according to the selection criterion of the optimized optical path difference.[29]

Table 1. Simulation parameters.

Targeted absorption line	Energy coefficient A	1
	Center wave number σ_1	1/413.260 nm^{-1}
	FWHM w_1	0.5855 cm^{-1} (0.01 nm)
	Absorption depth A_1	0.9
DASH interferometer	Center wavenumber of filter passband σ	1/413 nm^{-1}
	FWHM of filter passband w	58.6273 cm^{-1} (1 nm)
	Grating period p	1/1200 mm
	Littrow angle θ_{L}	14.25°
	Optical path offset $2\Delta d$	6.4 mm
	Number of detector pixels in a row N	1024
	Detector pixel size	13 μm

The filtered incident spectrum without Doppler shift is shown in Fig. 3, and its interferogram recorded by the detector is shown in Fig. 4(a). In Fig. 4(a), the intensity of the fringe at zero optical path difference ($L = 0$) is largest, and the interference fringe contrast decreases first rapidly and then gradually with the increase of optical path difference. Figure 4(b) displays the result of the Fourier transform of the interferogram shown in Fig. 4(a). Since the wave numbers of the incident spectral lines are smaller than the Littrow wave number of the grating, the frequency spectrum in the right half plane, as the

retrieved spectrum, is a mirror image of the filtered incident spectrum shown in Fig. 3.

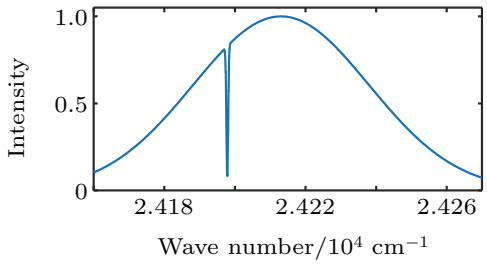

Fig. 3. Spectral density of filtered incident radiation without Doppler shift for single absorption line in passband.

The interference fringes near the zero optical path difference ($L = 0$) are due to the superposition of two sets of interference fringes with different spatial frequencies, where the interference fringe from the passband represented by B_0 is stronger and dominates. It is noted that since phase shift of interference fringe is proportional to the difference between their sampling optical paths, the phase shift at $L = 0$ is 0. It means that although the intensity of the interferogram at $L = 0$ is strongest, the inversion of the Doppler radial velocity cannot be performed here. Moreover, the central wavenumber of the retrieved spectrum shown in Fig. 4(b) is determined by the transmission function of the filter but not by Doppler shift, the phase shift caused by the Doppler shift of the absorption line thus cannot be obtained by processing the interferogram shown in Fig. 4(a) according to the data processing method for emission lines. Therefore, it is critical to find a way to effectively measure the Doppler shift of the absorption line in the passband.

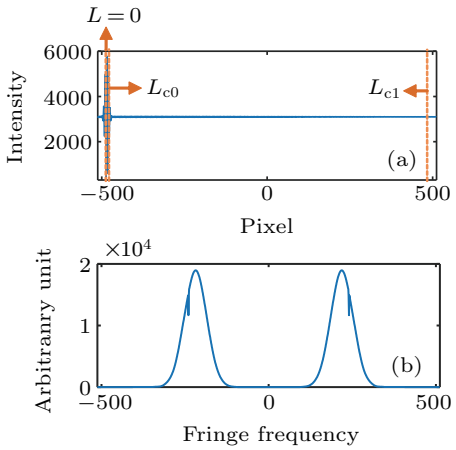

Fig. 4. (a) 1024-pixel detector recorded interferogram of radiation and (b) its Fourier transform, where the zero-frequency component is filtered out.

According to the analysis described in Subsection 2.1, the coherence length of B_0 is 9.0405×10^{-2} mm, and then the corresponding location on the detector is -477 calculated from $L = 4\tan\theta \times (x + \Delta d/2\tan\theta)$. Similarly, the coherence length of B_0B_1 is 12.80 mm, and then the corresponding location on the detector is 485. That is to say, theoretically, the interference fringes in the range of $-477 \leq x \leq 485$ on the detector can be regarded as being generated only by the absorption line in the passband. However, since the line energy of B_0 is much larger than that of B_0B_1, the interference fringes formed by B_0 at $x = L_{c0}$ still have a significant influence on the measurement of Doppler radial velocity. Therefore, considering the influence of B_0 on and the detector response to line light intensity, the interferogram data from the center half of the CCD ($-256 \leq x \leq 255$) as shown in Fig. 5(a) are extracted for subsequent data processing. Its Fourier transform is shown in Fig. 5(b). Figure 6 shows the retrieved phases *versus* pixel number from Fig. 5(b) by following the approach to treating a single emission line. We obtain the phase shift of 0.0324 rad at $x = 0$, and then the retrieved speed $v = 99.9855$ m/s according to Eq. (8). Comparing with our set Doppler radial velocity, the relative error is 0.0145%, which proves the feasibility of using a DASH interferometer for measuring the Doppler-shift of a single absorption line in the passband with high precision.

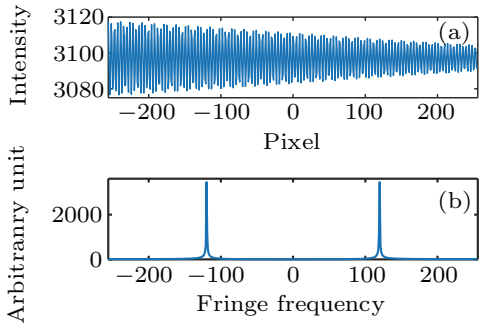

Fig. 5. (a) Interferogram of center 512 pixels in Fig. 4(a), and (b) its Fourier transform, where zero-frequency component is filtered out.

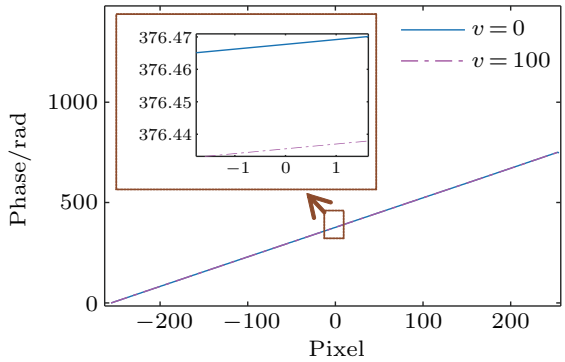

Fig. 6. Phase of interferogram shown in Fig. 5(a), where dark blue solid line indicates phase from Doppler-non-shifted interferogram and magenta dash-dotted line indicates phase from Doppler-shifted interferogram.

We further simulate the Doppler-shift measurements of multiple absorption lines in the passband, obtained with the same DASH instrument as that described in Table 1. The rest center wavelengths of the three absorption lines in the passband are assumed to be 412.725 nm (24229.2083 cm^{-1}), 412.755 nm (24227.4473 cm^{-1}), and 413.260 nm (24197.8416 cm^{-1}), respectively. The remaining parameters of the absorption lines are still described as those in Table 1. Doppler radial velocities are set to be 100 m/s for all three absorption lines.

The spectral density of filtered incident Doppler-non-shifted radiation is shown in Fig. 7, and its interferogram recorded by the detector is shown in Fig. 8(a). In the vicinity of $L = 0$, the interference fringes, whose intensity distribution with the optical path difference is nearly the same as the case of a single absorption line in the passband, are still largely determined by the transmission function of the filter. Figure 8(b) displays the Fourier transform of the interferogram shown in Fig. 8(a). Comparing with the spectrum shown in Fig. 7, we can find that the two adjacent absorption lines just cannot be distinguished here. This is because there are not enough sampling points, thus resulting in low spectral resolution.

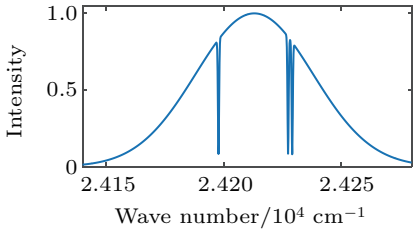

Fig. 7. Spectral density of filtered incident radiation without Doppler shift for multiple absorption lines in passband.

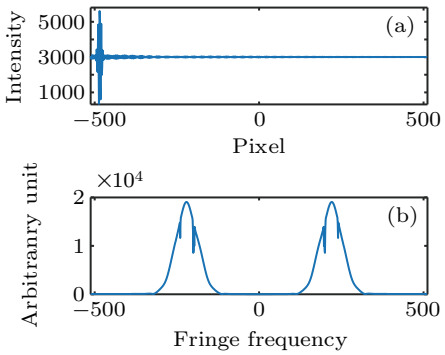

Fig. 8. (a) Interferogram of the radiation shown in Fig. 7, recorded by 1024-pixel detector, and (b) its Fourier transform, where zero-frequency component is filtered out.

With the numerical simulation of a single absorption line in the passband, the interference fringes in the central region of Fig. 8(a) ($-256 \leq x \leq 255$) are extracted and shown in Fig. 9(a). Figure 9(b) exhibits the Fourier transform of the interferogram shown in Fig. 9(a). In theory, there should be three positive frequency features in the frequency domain, but only two ('I' and 'II') are shown here. Because of low spectral resolution, the two adjacent spectral lines cannot be distinguished, and thus merging into one line and displaying the frequency feature'I'. Since the difference in central wavenumber between the two adjacent spectral lines is small and their Doppler radial velocities are the same, we can directly calculate the phase shift caused by the frequency shift of the frequency feature 'II' instead of trying to distinguish the two lines, and then isolate them for phase calculation. Next, isolate the frequency features 'I' and 'II' in the right half plane of Fig. 9(b) separately, then we will calculate their respective phases. For feature 'I', the calculated phase shift is 0.0325 rad, and the retrieved speed from Eq. (8) is 100.1188 m/s. For feature 'II', the calculated phase shift is 0.0323 rad, and the retrieved speed is 99.5679 m/s.

We note that compared with the Doppler radial velocities we set, the retrieved speed of feature 'I' has a relative error of 0.1188% and the retrieved speed of feature 'II' has a relative error of 0.4321%. The error of the feature 'I' is larger than that in the numerical simulation experiment for a single absorption line in the passband, which may be due to the approximate error of formula or the frequency aliasing with part of feature 'II'. The reason why the relative error of the retrieved speed of feature 'II' is larger than that of feature 'I' is that the frequency shifts of the two unresolved spectral lines treated as one spectral line feature are not exactly equal. Nevertheless, the error is very small, implying that it is feasible to treat the two unresolved absorption lines with the same Doppler radial velocity as one for phase calculation. In addition, we change the set Doppler radial velocities for the three absorption lines simultaneously while keeping other parameters changeless. Figure 10 shows the numerical simulation results. We can see that the relative errors of the retrieved speeds are less than 0.7% without considering the noise, demonstrating the feasibility of using a DASH interferometer to measure the Doppler-shift of multiple absorption lines in the passband with high precision.

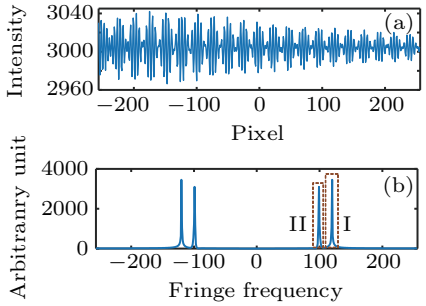

Fig. 9. (a) Interferogram of center 512 pixels in Fig. 8(a), and (b) its Fourier transform, where zero-frequency component is filtered out.

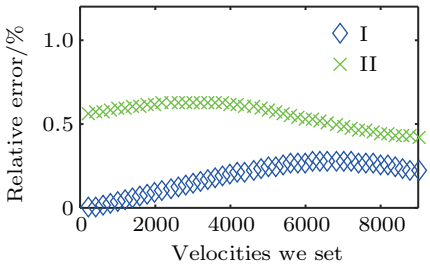

Fig. 10. Simulation results at different set Doppler radial velocities, where blue diamond represents relative error of retrieved speed of feature 'I', and green cross represents relative error of retrieved speed of feature 'II'.

4. Conclusions

In this study, we establish a mathematical model of the Doppler-shift measurements of absorption lines by a DASH interferometer. Aiming at the characterizing the absorption lines, the components of the interferogram received by the detector array are presented and analyzed in detail. In order to

obtain the phase shifts of the interference fringes, caused by the Doppler shifts of the absorption lines in the passband, we find that it is critical to obtain the interference fringes generated only by the absorption lines in the passband. Our study shows that the interference fringes generated by the absorption lines can be extracted and then be processed to obtain phases by the data processing method for emission lines. In the end, we carry out numerical simulation experiments. As expected, the simulation results are in good agreement with our theoretical analyses and the relative error of the retrieved speeds is less than 0.7% under ideal conditions, thus proving that the phase shifts caused by the Doppler shifts of the absorption lines can be calculated by the method of processing emission lines, and demonstrating the feasibility of using a DASH interferometer to measure the Doppler-shift absorption lines with high precision.

References

[1] Antreasian P G, Baird D T, Border J S, Burckhart P, Graat E J, Jah M K, Mase R A, McElrath T P and Portock B M 2005 *J. Spacecr. Rockets* **42** 394

[2] Ryne M, Graat E, Kruizinga G, Lau E, Martin-Mur T, Nandi S, Portock B, Haw R and McElrath T 2008 *AIAA/AAS Astrodynamics Specialist Conference and Exhibit*, August 18–21, 2008, Honolulu, Hawaii, USA, p. 7215

[3] Kikuchi F, Kono Y, Yoshikawa M, Sekido M, Ohnishi M, Murata Y, Ping J, Liu Q, Matsumoto K and Asari K 2004 *Earth Planets Space* **56** 1041

[4] Zhang W, Chen X, You W, Zhang W and Fang B D 2013 *Aerosp. Shanghai* **30** 32 (in Chinese)

[5] Woodman O J 2007 "An Introduction Inertial Navigation", University Cambridge, Computer Laboratory, 2007

[6] Kubota T, Hashimoto T, Sawai S, Kawaguchi J I, Ninomiya K, Uo M and Baba K 2003 *Acta Astronaut.* **52** 125

[7] Marini A E, Racca G D and Foing B 2002 *Adv. Space Res.* **30** 1895

[8] Bhaskaran S 2012 *Proceedings of the SpaceOps* 2012 *Conference*, June 11–15, 2012, Stockholm, Sweden, p. 1267135

[9] Hays P B, Abreu V J, Dobbs M E, Gell D A, Grassl H J and Skinner W R 1993 *J. Geophys. Res. Atmos.* **98** 10713

[10] Killeen T L, Wu Q, Solomon S, Ortland D, Skinner W, Niciejewski R and Gell D 2006 *J. Geophys. Res. (Space Phys.)* **111** A10S01

[11] Shepherd G G, Thuillier G, Gault W, Solheim B, Hersom C, Alunni J, Brun J F, Brune S, Charlot P and Cogger L 1993 *J. Geophys. Res. Atmos.* **98** 10725

[12] Gault W, Brown S, Moise A, Liang D, Sellar G, Shepherd G and Wimperis J 1996 *Appl. Opt.* **35** 2913

[13] Thuillier G and Shepherd G G 1985 *Appl. Opt.* **24** 1599

[14] Thuillier G and Hersé M 1991 *Appl. Opt.* **30** 1210

[15] Tang Y H, Cui J, Gao H Y, Qu O Y, Duan X D, Li C X and Liu L N 2017 *Acta Phys. Sin.* **66** 130601 (in Chinese)

[16] Zhang C M and Zhu L Y 2010 *Acta Phys. Sin.* **59** 989 (in Chinese)

[17] Mu T K and Zhang C M 2010 *Chin. Phys. B* **19** 060702

[18] Englert C R, Harlander J M, Babcock D D, Stevens M H, Siskind D E 2016 *Proceedings of the Atmospheric Optical Modeling, Measurement and Simulation II*, August 13–17, 2006, San Diego, California, USA p. 63030T

[19] Harlander J M, Englert C R, Babcock D D and Roesler F L 2010 *Opt. Express* **18** 26430

[20] Englert C R, Harlander J M, Emmert J T, Babcock D D and Roesler F L 2010 *Opt. Express* **18** 27416

[21] Babcock D, Harlander J, Englert C, Roesler F, Pedersen T and Feldman R 2009 *Proceedings of the AGU Fall Meeting*, December 14–18, 2009, San Francisco, California, USA, pp. SA53A-1251

[22] Babcock D D 2011 "Deveopment of a Space Flight Prototype Doppler Asymmetric Spatial Heterodyne (DASH) Spectrometer for the Measurement of Upper Atmospheric Winds", ARTEP INC ELLICOTT CITY MD, 2011

[23] Babcock D, Harlander J, Englert C, Roesler F, Pedersen T and Feldman R 2010 *Proceedings of the AGU Fall Meeting*, December 13–17, 2010, San Francisco, California, USA, p. SA11B–1586

[24] Englert C R, Brown C M, Bach B, Bach E, Bach K, Harlander J M, Seely J F, Marr K D and Miller I 2017 *Appl. Opt.* **56** 2090

[25] Englert C R, Harlander J M, Brown C M, Marr K D, Miller I J, Stump J E, Hancock J, Peterson J Q, Kumler J and Morrow W H 2017 *Space Sci. Rev.* **212** 553

[26] Harlander J M, Englert C R, Brown C M, Marr K D, Miller I J, Zastera V, Bach B W and Mende S B 2017 *Space Sci. Rev.* **212** 601

[27] Harding B J, Makela J J, Englert C R, Marr K D, Harlander J M, England S L and Immel T J 2017 *Space Sci. Rev.* **212** 585

[28] Englert C R, Babcock D D and Harlander J M 2007 *Appl. Opt.* **46** 7297

[29] KuangY L, Fang L, Peng X, Cheng X, Zhang H and Liu E H 2018 *Acta Phys. Sin.* **67** 140703 (in Chinese)